GEOPHYSICS, VOL. 74, NO. 5 (SEPTEMBER-OCTOBER 2009); P. B139–B151, 20 FIGS., 1 TABLE.
10.1190/1.3157461

Case History

2D seismic exploration of the Ancona landslide (Adriatic Coast, Italy)

Eusebio Stucchi[1] and Alfredo Mazzotti[2]

ABSTRACT

We have used on- and offshore seismic reflection profiles to determine the extension of a historic landslide at depth and toward the sea. The subsurface landslide structure was delineated by using four separate data sets produced by the combined use of geophone and hydrophone spreads, and of explosive and air-gun sources which also illuminated, through an undershooting configuration, the subsurface below the coastal road and railway. Many noise problems related to the source and environment were overcome and alleviated with several signal-processing routines. The resulting stack and depth-migrated sections reveal the deep geometry of the main landslide body and indicate the emergence location, at the landslide foot, of a deep, potential detachment surface, which previous investigations failed to evidence.

INTRODUCTION

Several locations of the geologically young Italian peninsula are affected by slope instability phenomena. In addition to the mountain areas of the Alps and Apennines, tracts of the Adriatic and Tirrenian coasts are affected by landslides (Cancelli et al., 1984), some of which are very large. One of the best known is the Ancona landslide, located immediately westward of the harbor city of Ancona. It is an ancient landslide, discovered in 1700, and covers an area of about 3.5 km^2 with a landslide front of about 2 km (Figure 1).

The geology of the area (Calamita and Deiana, 1986; Ciancetti et al., 1986; Cotecchia, 1997) is characterized by a sequence of marly clays stratified with silts and sands of the lower and middle Pliocene, covered by silty clays interbedded with thin sandstone layers of Pleistocene age in a transgressive order. Alluvial and colluvial clays and silts are deposited on top. The tectonic activity in the Adriatic side of the Apennines was intense during the Pliocene and Pleistocene, with a strong uplift of the Quaternary sediments to more than 250 m above sea level (a.s.l.). The Montagnolo hill, which will be mentioned in the following sections because it is an end location of the seismic acquisition, is an expression of such tectonic activity.

The main tectonic lineaments are oriented along and across the Apenninic trend (northwest–southeast or northeast–southwest). Morphologically, the area is characterized by an average slope of about 10° with several successions of scarps, trenches, and counter slopes (Coltorti et al., 1986). These features are typical of deformed slopes, where large periodical landslides occur.

In recent times, the most severe event took place on 13 December 1982, when more than 300 buildings were strongly damaged, including a hospital and some university structures. The Adriatic railway and the Flaminia road were disrupted (Figure 2), as well as water and gas pipelines. The fast movement started almost simultaneously in every point of the area and terminated in about two hours. A maximum vertical displacement of 6 m (uplift along the coast) and a maximum horizontal displacement of 11 m were recorded.

Despite extensive engineering and geologic investigations, which were carried out in the period immediately following the 1982 landslide (Bernardini et al., 1986; Bianco, 1986; Ciancetti et al., 1986; Cotecchia, 1997), some relevant aspects still remained somewhat unclear. For instance, the geometry of the major landslide body was not determined fully. In particular, the maximum depth of the potential sliding surface and its emergence location at the landslide foot were not clear. In some hypotheses based on landslide models, the landslide foot was predicted as far as 200–250 m offshore (Cotecchia, 1997).

Refraction and downhole seismic investigations were carried out on land (Cassinis et al., 1985; Bernardini et al., 1986; Cassinis et al., 1986). These studies characterized the shallow portions of the landslide, evidencing the presence of lateral velocity discontinuities and a vertical structure constituted of at least three layers with increasing velocity. Approximately 200 m offshore, two separate high-resolution seismic reflection surveys were performed (Curzi and Stefanon, 1986; Cotecchia, 1997) to get a more detailed insight of the area facing Ancona. These data helped to delineate the seaward shallow structure of the area (Tavernelle syncline, Ciancetti et al., 1986; Cotecchia, 1997) but did not show any detachment surface or recent

Manuscript received by the Editor 5 August 2008; revised manuscript received 20 February 2009; published online 21 August 2009.
[1]University of Milan, Department of Earth Sciences — Geophysics, Milan, Italy. E-mail: eusebio.stucchi@unimi.it.
[2]University of Pisa, Department of Earth Sciences — Geophysics, Pisa, Italy. E-mail: mazzotti@dst.unipi.it.

deformations of the layers, indicating that the sliding action had terminated, it would seem, somewhere nearer to the coast in a yet unknown location.

The objective of our survey was to delimit the extension of the landslide at greater depth and toward the sea because this was a key point for planning the consolidation work and quantifying the related costs. For example, the design of the bank to be put at the landslide foot, and, in particular, its proper dimensioning and positioning, required accurate knowledge of the emergence location of the sliding surface. To this end, we applied high-resolution seismic reflection to investigate the landslide zone and used satellite radar interferometry to monitor the surface displacements in the framework of two research projects.

We designed a P-wave high-resolution seismic line crossing the entire landslide body, from sea to land, filling the gap between the existing grid of marine lines and the coastline, where we presumed the landslide foot was located. The direction of this new profile was orthogonal to the coast and to the visible trenches (orientation north–south, Figure 1).

A detailed description of the seismic acquisition and of the types of noises and problems encountered is given in Stucchi, Zgur, and Baradello (2005), and the radar interferometry results are discussed in other papers (Mazzotti and Rocca, 2003; Rott et al., 2003).

Few works are available that deal with seismic reflection applied to the study of slope instability phenomena and in particular with the data acquisition and processing. Examples of land seismic reflection investigations with environmental conditions that are very different from our case study can be found, for example, in Bruno and Martillier (2000), Brückl et al. (2001), and Bichler et al. (2004). Martinez et al. (2005) and Schnellmann et al. (2006) present seismic studies on marine landslides, but these studies are focused mainly on interpretation. To our knowledge, no published work deals with a joint land-marine seismic investigation of landslides. Therefore it is of interest to discuss the crucial steps of the seismic data processing of this land-marine seismic line, up through the production of the depth-migrated section, and to illustrate the main outcomes in terms of the inferred geometry of the landslide body. In particular, this study demonstrates that, notwithstanding the very difficult environmental conditions, the combined marine-land seismic exploration has produced a detailed depth image of the rock bodies and rupture surfaces.

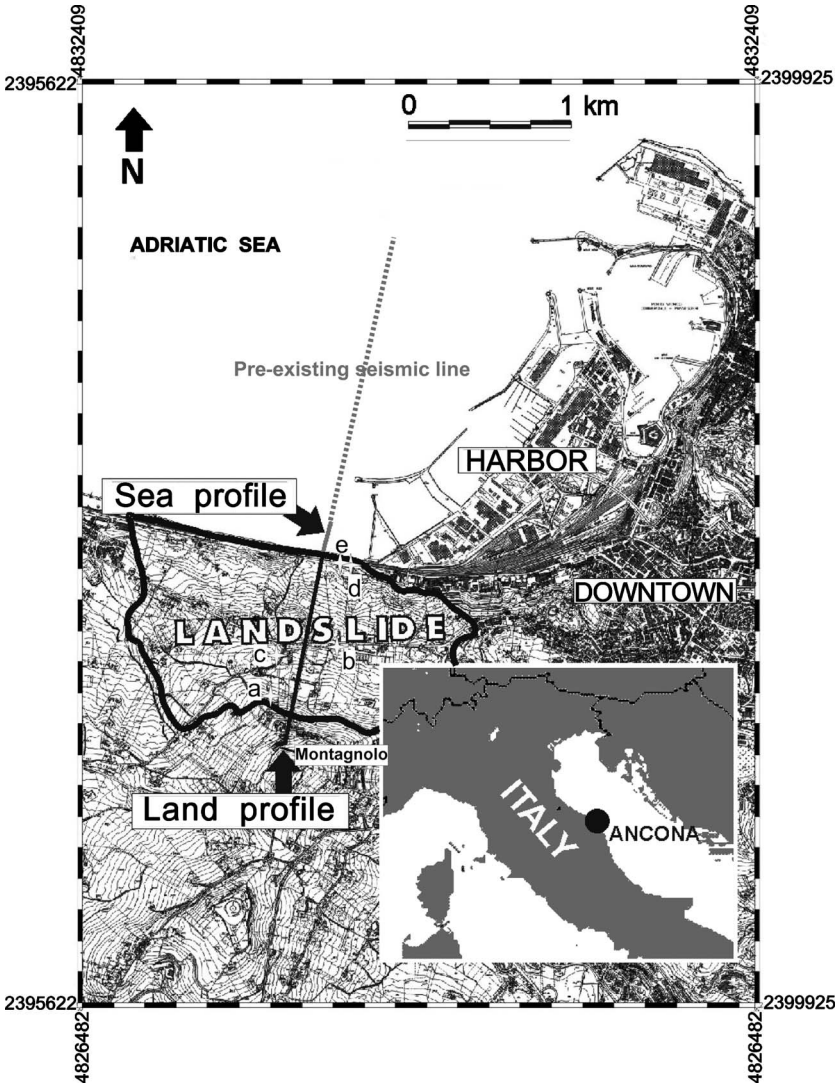

Figure 1. Map of the Ancona landslide area with the location of the new land-marine seismic line that crosses the landslide body approximately from north to south. The new profile starts 240 m offshore (to the north) and arrives close to the Montagnolo locality (241 m a.s.l. to the south). Shown also are the position of a pre-existing marine seismic line (dotted line) that represents the progression toward the sea of the newly acquired profile and locations where the pictures in Figure 2 were taken.

METHODOLOGY

Field data: Acquisition and main characteristics

The seismic profile is about 1500 m long, 240 m offshore, and 1300 m onshore. We planned the survey to cross the whole landslide slope, from the apical part in the Montagnolo area (251 m a.s.l.) through the landslide foot located in a (to be discovered) position between the land coastal area and farther offshore. The requirements for the acquisition were to ensure (1) continuous subsurface coverage from sea to land despite the crossing of the Adriatic railway and the Flaminia road; (2) depth of investigation sufficient to reach detachment surfaces which, according to some hypotheses based on geologic and engineering models, could be as deep as 300 m below the surface; and (3) high common-midpoint (CMP) fold (minimum 4800%) for land and marine data.

These requirements led us to use a bay-cable streamer of 48 hydrophones, firmly anchored to the seafloor and connected to a land acquisition system of as many as 152 active channels. The simultaneous recording of land shots by the bay-cable hydrophones, and of air-gun shots by the geophone spread in an undershooting configuration,

allowed us to record data below the coastal roadand railway where we could not place any shooting or recording device.

The group interval of 5 m for both the hydrophone and geophone stations resulted in source-receiver offsets between 400 m and 500 m, depending on how many channels were online. We used circular arrays of six closely spaced geophones at each land station to enhance the signal-to-noise (S/N) ratio. We used small explosive charges (150 g) in 3-m-deep boreholes and alternatively two types of air gun (0.66 l and 1.32 l) as energy sources. Both air-gun types were single gun with no bubble-suppression device. We achieved the minimum nominal coverage of 4800% for land shooting, despite the low accessibility to some places (trenches), whereas we recorded more than 300 air-gun shots during marine acquisition. Sample interval and record length were 0.5 ms and 1 s, respectively.

Figures 3 and 4 show examples of field-shot gathers representative of the average data quality along the profile. Figure 3 shows the close-up of a common-source gather acquired with the 0.66 l air gun and recorded simultaneously by the geophone and hydrophone spreads. Note the dead traces from channels 49 through 57 corresponding to the intersection of the Adriatic railway and the Flaminia road with the seismic spread. The data recorded by the hydrophones are displayed on the left (channels 1–48), and the data recorded by the geophones are displayed on the right (channels 58–152).

Three kinds of noise are clearly visible. First, a low-velocity, low-frequency, high-amplitude, and dispersive wavetrain is visible, originating at the source position and with characteristics very similar to the ground roll. Then a duplication of all the recorded signals is visible (see, for example, the first arrivals), which results from the bubble effect of the single air gun. Finally, bands of high-frequency noise affect all the land data, and their duration varies between 100 and 250 ms or more. This kind of noise is caused by the vicinity of high-power broadcasting antennas transmitting electromagnetic signals that interfere with the seismic recording equipment. Unfortunately, the lower frequencies of their spectrum overlap with the signal bandwidth; thus they cannot be easily filtered out.

Figure 4 shows the close-up of a shot gather acquired with the explosive source. The shot position in this case was too far from the coastline to activate the by-cable hydrophones, and therefore the data shown were recorded by the geophones only. High-amplitude reverberations resulting from guided waves (indicated in the figure) follow the first arrivals and last as long as 150–200 ms. They are particularly troublesome because they interfere with the shallow reflections in the time-offset window left undisturbed by the low-velocity, dispersive ground roll. The electromagnetic noise generated by the broadcasting antennas is present again, but note that its time occurrence varies randomly from one shot to another (see Figures 3 and 4), and its moveout always is zero.

To give an idea of the typical ambient noise that characterized the acquisition site, Figure 5 illustrates a no-shot record with the same spread loca-

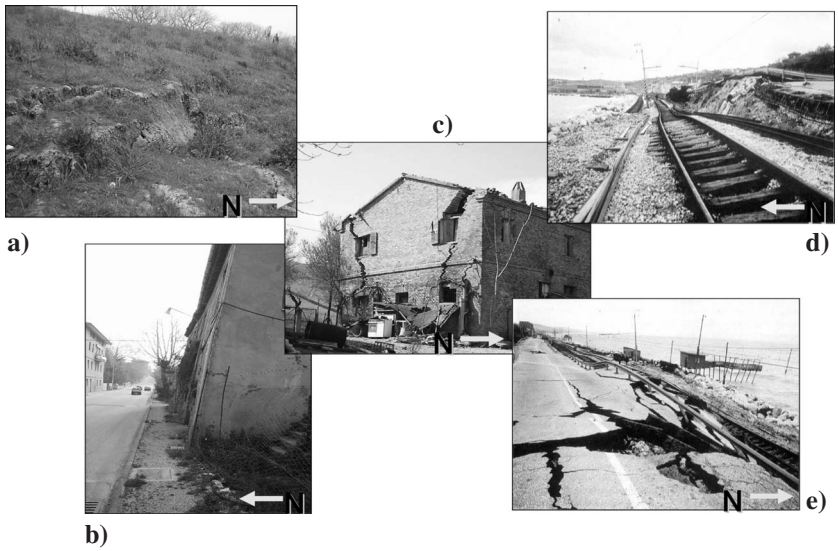

Figure 2. Some examples of the damage caused on 13 December 1982 (some pictures taken from Cotecchia, 1997). Note in (e) and (d) the disruptions of the Flaminia road and the Adriatic railway.

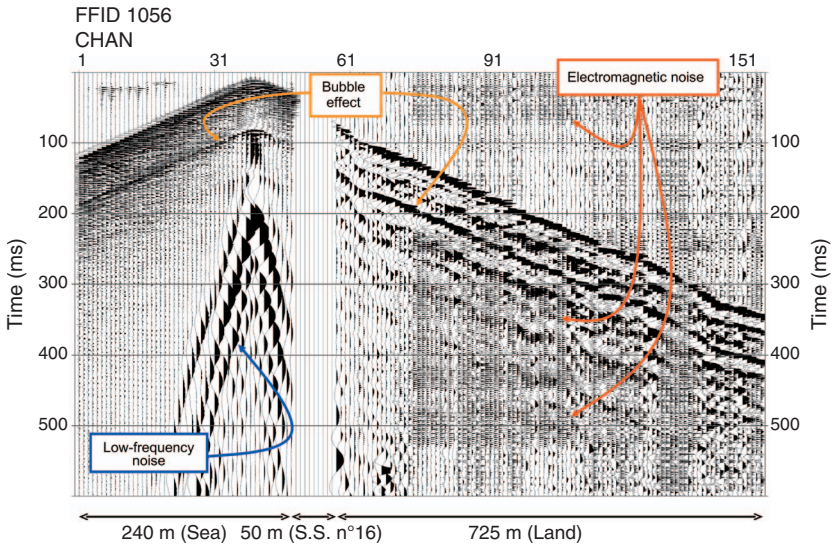

Figure 3. Example of a typical field shot gather (field file identification number FFID 58) acquired with the 0.66 l air gun and recorded simultaneously by the geophone and hydrophone spreads. On the left are the data recorded by the hydrophones (channels 1–48); on the right are the data recorded by the geophones (channels 58–152); in between are the dead channels corresponding to the Flaminia road and the Adriatic railway. Three kinds of noises are indicated also: the surface waves, bubble effect, and noise resulting from electromagnetic interference with the recording equipment.

tion as that in Figure 3. Note the high amplitudes of the noise contaminating the traces closer to the Flaminia road and to the railway (100 times greater than any other kind of noise present in the data). Note also the presence of the high-frequency electromagnetic noise on the land channels (58–151), and of the low apparent-velocity surface waves generated by vehicles in transit along the coastal road. Unlike many other cases (see later in the text), the hydrophone traces (1–48) of this specific record were not particularly affected by coherent noise caused by marine activities.

We recorded four data sets as a function of energy source and recording sensors: air gun as energy source and hydrophones as recording devices, named marine-marine data; air gun as energy source and geophones as recording devices, named marine-land data; explosive charges as energy source and hydrophones as recording devices, named land-marine data; and explosive charges as energy source and geophones as recording devices, named land-land data. The marine-marine and marine-land data sets could be subdivided further, depending on whether we used the small 0.66 l air gun or the 1.32 l air gun.

Within the research projects, we analyzed and processed the different data sets, but we discuss here the procedures and results pertaining to the data sets marine-marine, land-marine, and land-land. These correspond to the data that yielded the best results. In the end, the marine-marine data used are those acquired with the small air gun of 0.66 l because the bubble effect was less severe and because they yielded a more detailed image of the shallow reflectors. The marine-land data, in which we initially had high expectations, especially in view of the relevant number of air-gun shots recorded by the geophones, proved to be very troublesome because of the deleterious combination of the bubble effect, geophone response, and land noise.

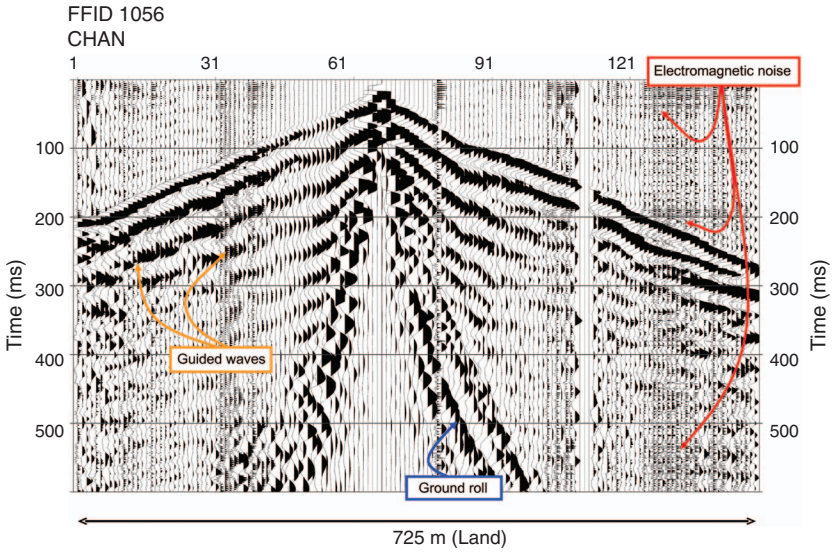

Figure 4. Close-up of a shot gather acquired with the explosive source. The data are recorded by the geophones only. In fact, the shot position is too far from the coastline to activate the hydrophone channels. Some recorded noises such as ground roll, guided waves, and electromagnetic noise are indicated.

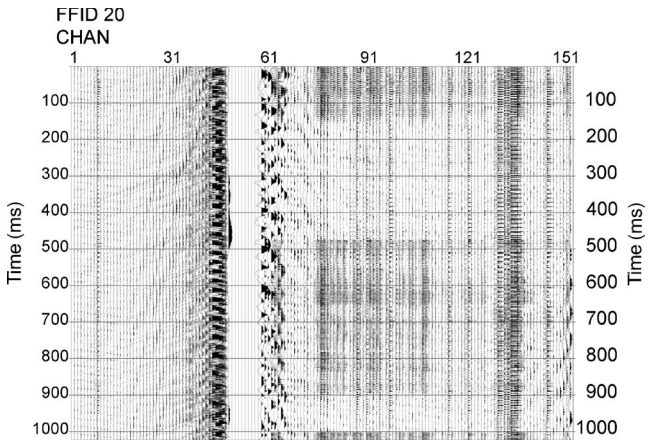

Figure 5. Example of noise test acquired with the spread in the same position as that in Figure 3. Note the high-amplitude values caused by the coastal road traffic and the presence of the electromagnetic noise bands on the land-recorded data only.

Detailed inspection of the field records, such as those shown in Figures 3 and 4, indicated that the processing required tailoring to each combination of sources and sensors with which we recorded the data. This is because of significant differences in the explosive-air-gun source wavelets and in the hydrophone-geophone responses, emphasized by the different coupling conditions and noises present on- and offshore.

The scheme of Table 1 summarizes the processing sequence for each kind of data. In what follows, not all the steps of processing that were applied have been described, because many of them are standard, well-known operations (Baker, 1999; Yilmaz, 2001). Instead, the focus is on the crucial problems and how to solve them. The main processing issues we faced were (1) the removal of the various kinds of noise in the data, (2) the computation of the static corrections along a corrugated profile with a height difference of nearly 250 m in 1500-m line length, and (3) the depth migration of the final data.

Noise removal

Noise caused by the broadcasting antennas

The data recorded on land were affected by the high-frequency — and apparently coherent — noise (Figure 6a) generated by the broadcasting antennas located nearby the acquisition site. Because of the overlapping of the signal and noise spectra, no simple band-pass filter could be applied to remove the noise without harming the high-frequency end of the signal spectrum. In fact, spectral analyses of the data indicated that the electromagnetic noise extended below 150 Hz. After several tests, including band-pass and singular value decomposition (SVD) filtering, we finally achieved a satisfactory noise attenuation using FX deconvolution.

We carried out a first step of FX prediction on the shot-gather data, along overlapped temporal windows in a frequency range of 125 Hz-open. This operation estimated those noise components at the high end of the frequency spectrum with null or very limited moveout. On the other hand, signal data were not recognized as predictable and thus did not appear in the estimation. We then subtracted the estimated noise from the data. Figure 6b and d shows the final results of this procedure. In the displayed shot gather, the attenuation of the

electromagnetic noise is satisfactory at all times (compare Figure 6a and b); correspondingly, in the frequency domain the spectral components above 125 Hz, and correlated to the electromagnetic noise, are effectively reduced (see Figure 6c and d).

Air-gun bubble

The first problem we faced with the marine-marine data was the removal of reverberations connected with the bubble pulse of the single air guns, which were not equipped with any bubble-suppression device. Although we used the data relative to the smaller air gun of 0.66 l, the bubble effect still was significant. We tried two approaches. The first one made use of knowledge of the nominal signature of the air gun. Based on that, we computed a Wiener deconvolution operator that shaped the theoretical air-gun response to a desired "bubble-free" signature. However, although this approach worked perfectly for the treatment of the theoretical response, it was not as effective in treating the real data. This probably was the result of variations of the actual source signature during the acquisition, when more than 150 shots were produced in just a few hours for each air gun. This high rate of shooting probably caused variations in the temperature and pressure of the air gun and/or other unknown equipment problems, which led to the signature instability.

So, we had to resort to the application of standard, single-trace, predictive deconvolution with parameters defined on the basis of the trace autocorrelations, which varied from shot to shot, demonstrating the source instability. We needed two steps of deconvolution to attenuate the first and second bubble pulses. For the first step, prediction distances and operator lengths varied in the different recordings from 48 through 56 ms and from 18 through 20 ms, respectively. For the second step, prediction distances and operator lengths ranged from 105 through 120 ms and from 10 through 15 ms, respectively.

Figure 7a and b show an example of a marine-marine shot gather before and after the predictive deconvolution: a good attenuation of the bubble pulse is achieved for most of the traces. In those cases, especially for near-offset traces, when we judged the deconvolution results not satisfactory, we performed local muting operations to remove the data still affected by residual bubble effects. We also obtained a further reduction of short-period reverberations by predictive deconvolution applied to the poststack data.

Surface waves and guided waves

Surface-wave noise affects both geophone and hydrophone recordings and is clearly visible in Figures 3 and 4. We simply removed the noise on the hydrophone recordings by applying a high band-pass filtering (24–36 Hz-open) to the data (Figure 8a and b), and reflections, indicated by the arrows in Figure 8b, started to become visible.

Instead, time-variant band-pass filtering was not as effective in attenuating the ground roll on the geophone recordings; thus we needed to add a further step of partial muting of the shot-gather traces, which still were contaminated by remnants of surface waves. No *f-k* filtering was applied because of the strongly aliased nature of the ground-roll noise.

In those unfortunate cases when the surface waves were caused by approaching trucks rolling along the coastal road, the traces record-

Table 1. Flowchart of the processing sequence.

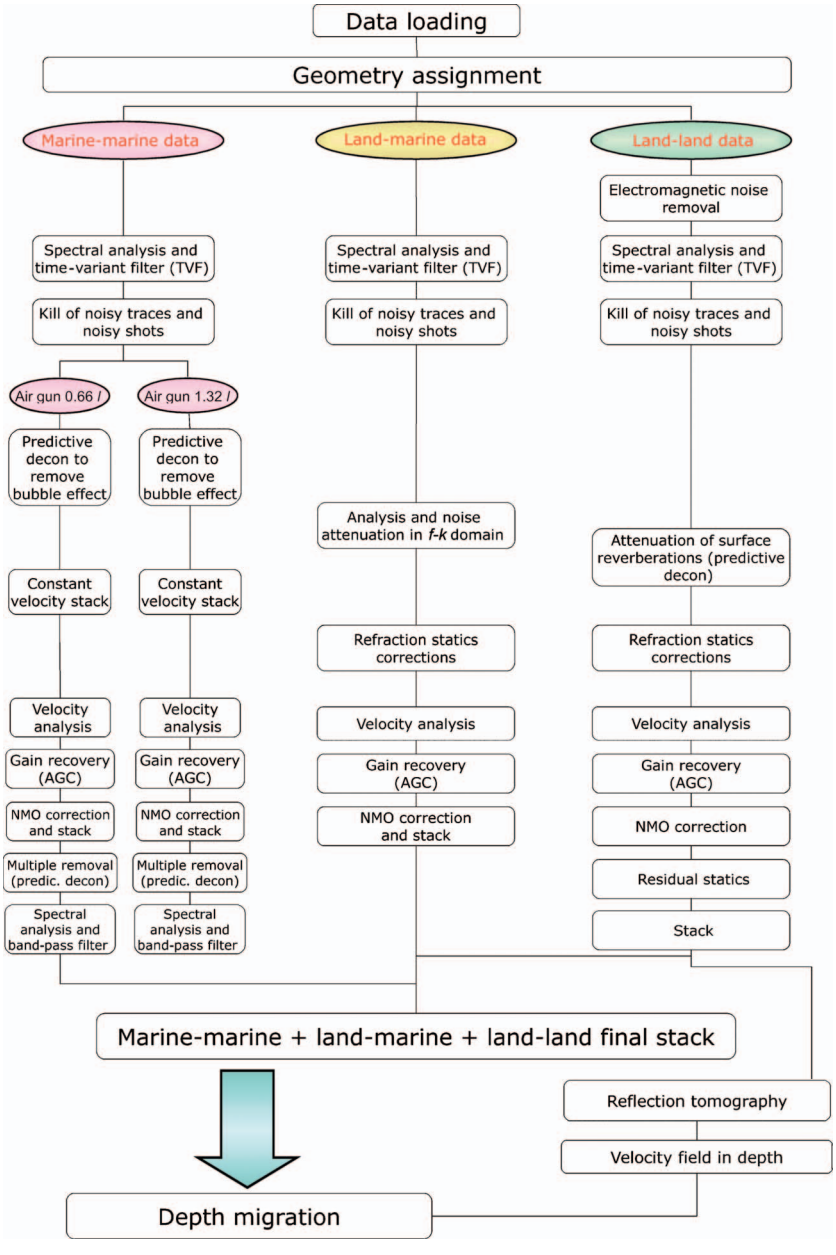

ed closer to the road, and sometimes entire shot records, had to be zeroed.

Many land-land shot records also were affected by guided waves replicating the first-break arrivals and thus interfering with the expected signal window. We achieved their effective attenuation by applying a predictive deconvolution with an operator length of 70 ms and a prediction distance of 10 ms.

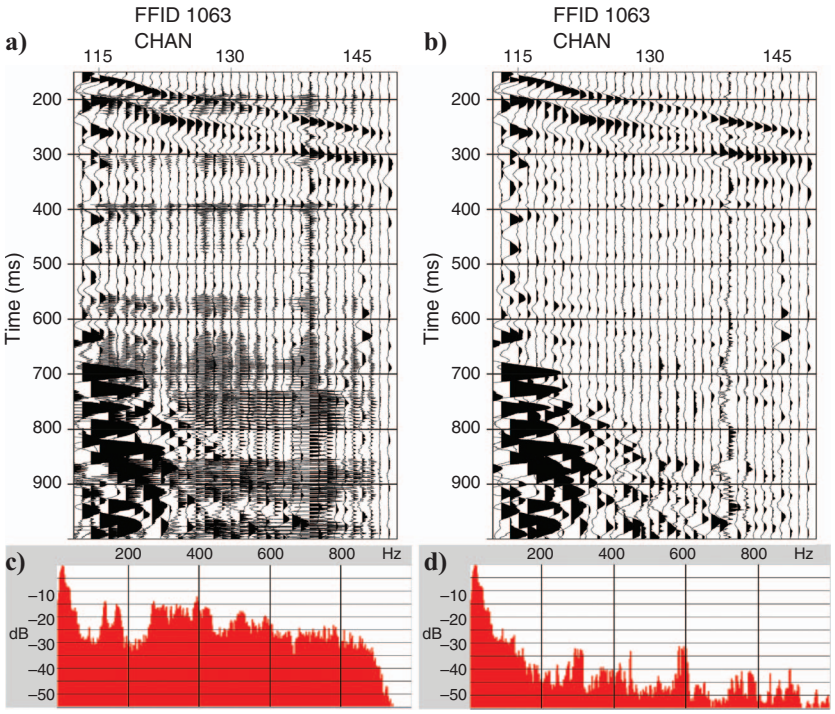

Figure 6. (a) Close-up of a shot gather evidencing the electromagnetic noise. (b) Results of the FX prediction and subtraction procedure. The noise suppression is quite satisfactory, as can be appreciated also on the Fourier spectra shown in (c) and (d) for the (a) original and (b) processed data, respectively.

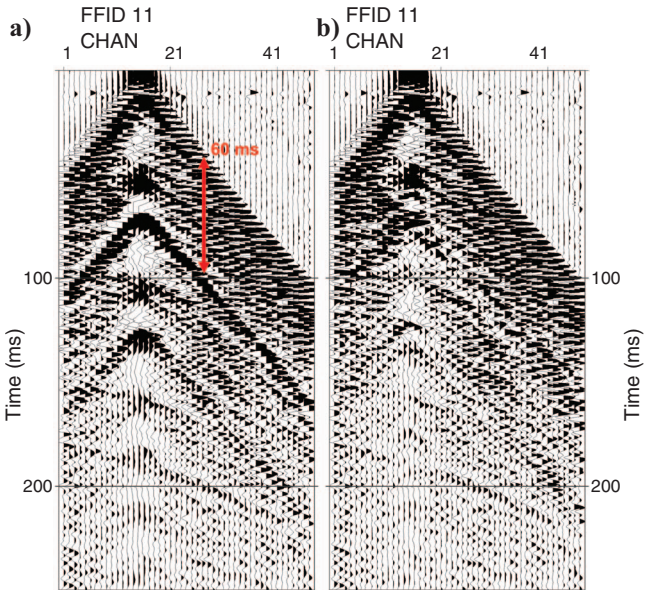

Figure 7. An example of a marine-marine shot gather (0.66 l air gun) (a) before and (b) after the predictive deconvolution applied to attenuate the bubble pulse. At short offset, when we considered the results unsatisfactory, we performed a local mute.

Passing ships

Ancona harbor is quite close to the acquisition site, and consequently strong coherent noise generated by incoming and exiting ships contaminated the hydrophone records, manifesting itself as dipping events, with dips opposite to the first breaks (Figure 9a). Having mapped the data into the *f-k* domain, it resulted that this type of coherent noise, having a negative apparent velocity, was separated from the signal and was not spatially aliased because of the small spatial sampling of 5 m. Thus we easily accomplished its removal through *f-k* filtering with no, or little, harm to the signal (Figure 9b).

The results of the prestack noise attenuation can be assessed by examining the shot gathers of Figures 10 and 11, which correspond to the same field records shown in Figures 3 and 4. The S/N of the data is increased greatly, and some reflection events (indicated by the black arrows), which were previously hidden by strong noise, now are visible. Similar considerations can be made by looking at some common-depth-point (CDP) gathers of the land-land line segment shown in Figure 12, (a) before and (b) after the denoising process. Both the original data of Figure 12a and the denoised data of Figure 12b have been normal-moveout (NMO) corrected with the same velocities to better reveal the presence of possible coherent reflections. The S/N improvement is significant. Other operations, such as stacking and poststack deconvolution, would attenuate further the residual noise present in the data.

After the noise-removal steps, the processing of the marine-marine, land-land, and land-marine records continued separately because of the still-manifest data differences. In addition, for marine-marine data no static corrections were needed

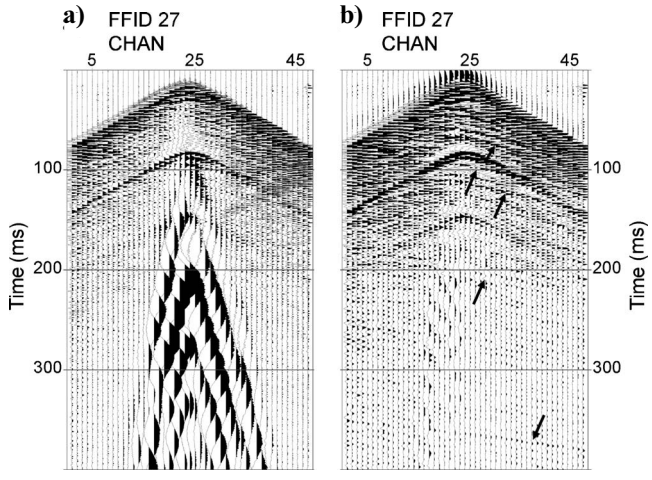

Figure 8. The low-frequency, low-velocity, high-amplitude surface waves (a) generated during the marine survey. They result from the shallow water depth and thus the short gap between the seabed and the air gun. This noise can be removed easily (b) by applying a high band-pass filter. The arrows indicate some possible reflections.

(apart from a constant shift to correct for the depth of the hydrophone cable), whereas they were very important for the land-land and land-marine records.

Static corrections and stack

The necessity of computing accurate static corrections results from several reasons such as the seaward-dipping-surface topography, with nearly 250 m of elevation difference between the highest and lowest (at sea level) stations, i.e., approximately the same distance as the presumed target depth; the heterogeneous nature of the surface sediments; and the corrugated topography along the seismic line, with elevation differences between nearby stations of several meters. To this end, we determined a model of the shallow subsurface by means of refraction-arrivals inversion. The first-break picking, apart from the time needed to perform it, was carried out easily because arrivals manifested themselves as clear kicks. We assumed a one-refractor model, and the result obtained is shown in Figure 13. The computed refractor velocity ranges from 1650 through 1740 m/s, whereas the weathered velocity is close to 850 m/s.

To maintain a good resolution in the subsequent velocity analysis, we computed and applied the static corrections first to a floating datum and then to a final, flat datum. The floating datum (red curve in Figure 14) is shown by a straight line that interpolates the topography (the maximum difference between the floating datum and the topography is 21 m). The final datum is located at an elevation of 250 m a.s.l. The blue curve in Figure 14 shows the corrections to the floating datum for each station: they vary from +8 ms through −20 ms. We performed the velocity analysis and the NMO correction after application of the statics to the floating datum, and then we moved the data to the final datum using the refractor velocity as replacement velocity. To appreciate the importance of the static corrections, Figure 15 shows the stack sections of the land-land data, obtained with the final stacking velocity field, (a) before the application of the statics to the floating datum, (b) after their application, and (c) after a final correction of residual statics. The progressive increase of the continuity of the reflectors is evident, and the deep synclinal structure on which the landslide body is seated starts to become visible.

In an undershooting configuration, the reflections in the land-marine data illuminate the subsurface below the Flaminia road and the railway, where no receivers or sources could be placed. The final stack section at the flat datum, which includes all the data (land-land, land-marine, and marine-marine), is shown in Figure 16. Shallow events, which on the land-marine data were recorded at short times and at great offsets, suffered an excessive NMO stretching and the consequent mute produced the absence of data between CDP 896 and 953 above 400 ms.

We applied other processing steps to all data sets, such as automatic gain for amplitude recovery (windows of 200 ms or 50 ms for very shallow marine data), constant velocity stacks as a testing tool before the semblance-velocity analysis, and time-variant filtering in pre- and poststack domain. Attempts to bring the different wavelets of the marine-marine, land-land, and land-marine data sets to a common, high-resolution wavelet were tried both pre- and poststack but with no success. In fact, in addition to the removal of the different impulse responses of receivers, we attempted several operations such as matched filtering, shaping deconvolution, and SVD wavelet estimation followed by deterministic deconvolution. However, the

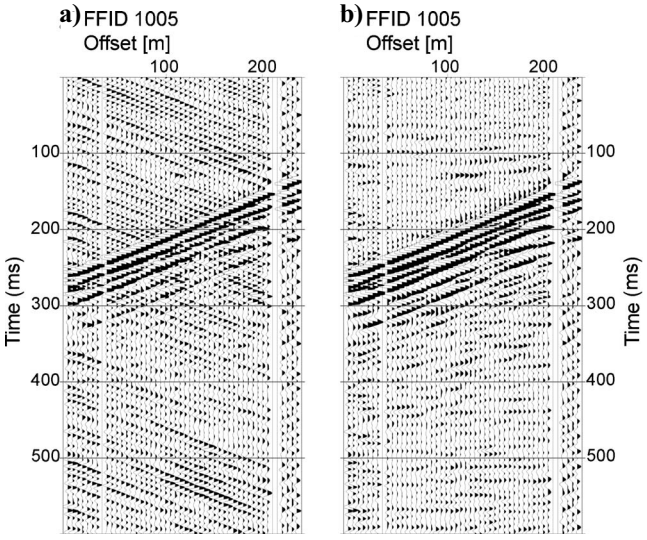

Figure 9. An example of a shot gather strongly contaminated by the noise coming from activities in the Ancona harbor. This noise manifests itself as (a) dipping events with dips opposite the first breaks; the high spatial sampling (5 m) allows its removal (b) by means of *f-k* filtering.

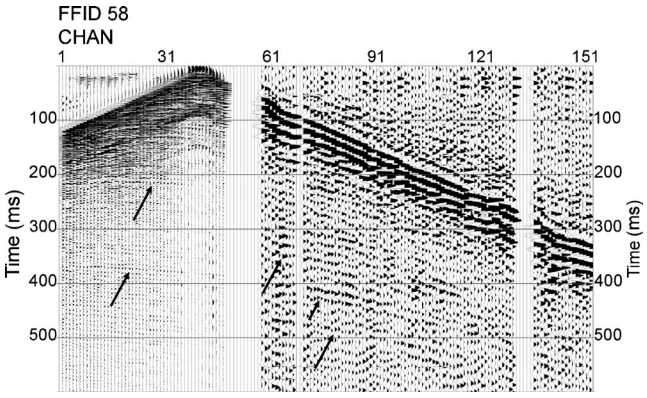

Figure 10. Same marine-land shot record as in Figure 3 at the end of the denoising operation described in the text. Some reflections that previously were hidden by the noise can be observed now and are indicated by the black arrows.

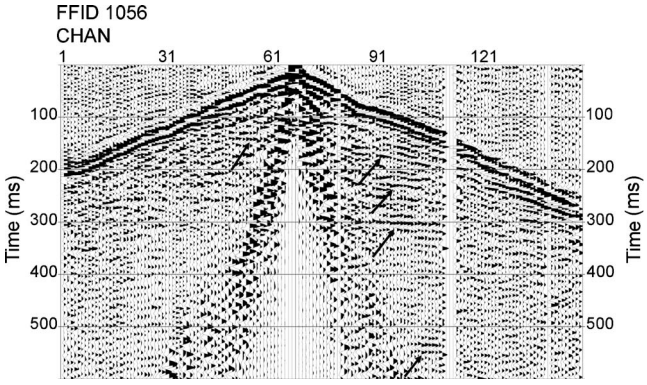

Figure 11. Same land-land shot record as in Figure 4 at the end of the denoising operation. Some reflections become evident (pointed to by the black arrows). We muted the residual of the ground roll still present at short offsets.

overwhelming effects of the different types and levels of noise, different source wavelets and coupling conditions, and different subsurface (chaotic on land, smooth and stratified offshore) prevented any significant success. In other words, the narrow-band noise-contaminated land-land data could not be enhanced to match the spectral characteristics of the wider-band higher S/N marine-marine data.

Therefore, although at the end of the time-processing sequence, the different characteristics of the data still are evident. The marine-marine stack (CDP 802–895, right-hand side of Figure 16) is the one showing the higher resolution, better coherency of reflectors, and greater depth penetration. This is mostly because of the very high fold (as high as 11,000%) of the CMP stack, the quieter recording en-

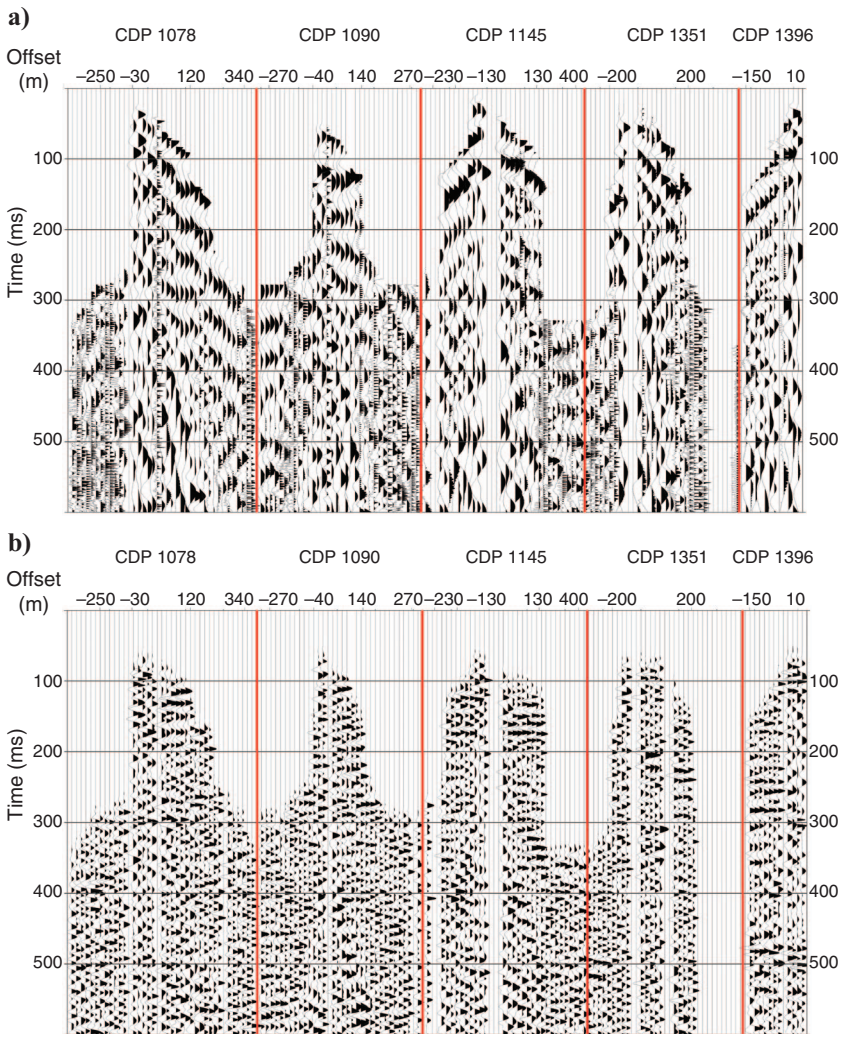

Figure 12. Some CDP gathers of the land-land profile (a) before and (b) after the noise removal operations. The data have been NMO corrected. Note the coherent, horizontally aligned segments of reflections that appear after the denoising process.

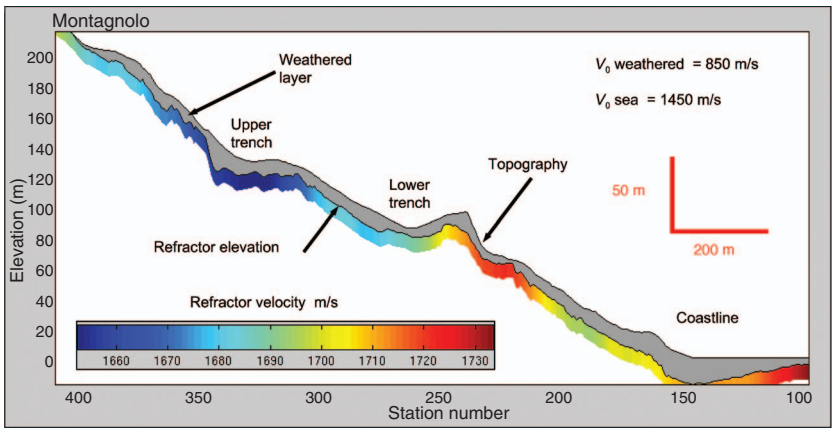

Figure 13. The one-refractor model of the subsurface computed by the inversion of the refraction arrivals. The weathered velocity is about 850 m/s, and the refractor velocity ranges from 1650 through 1740 m/s.

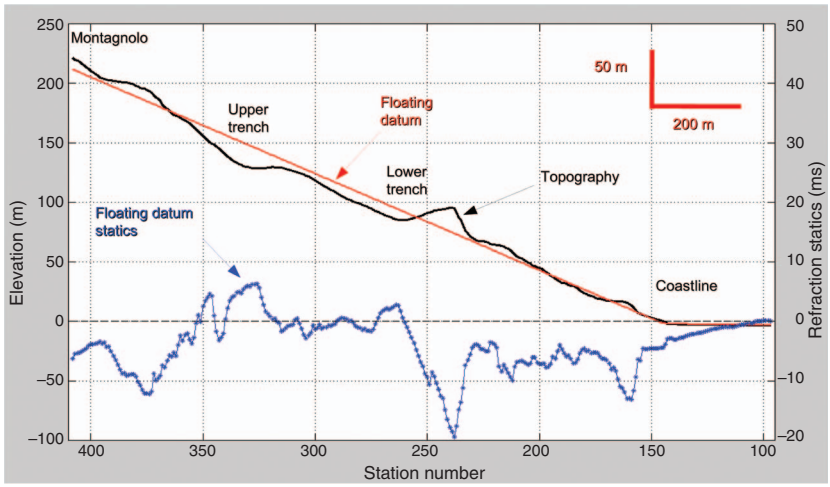

Figure 14. Topography of the seismic profile (black curve), floating datum (red curve) used to compute the static corrections, and the computed statics to the floating datum (blue curve). The trend of the static correction follows the difference between the topography and the floating datum.

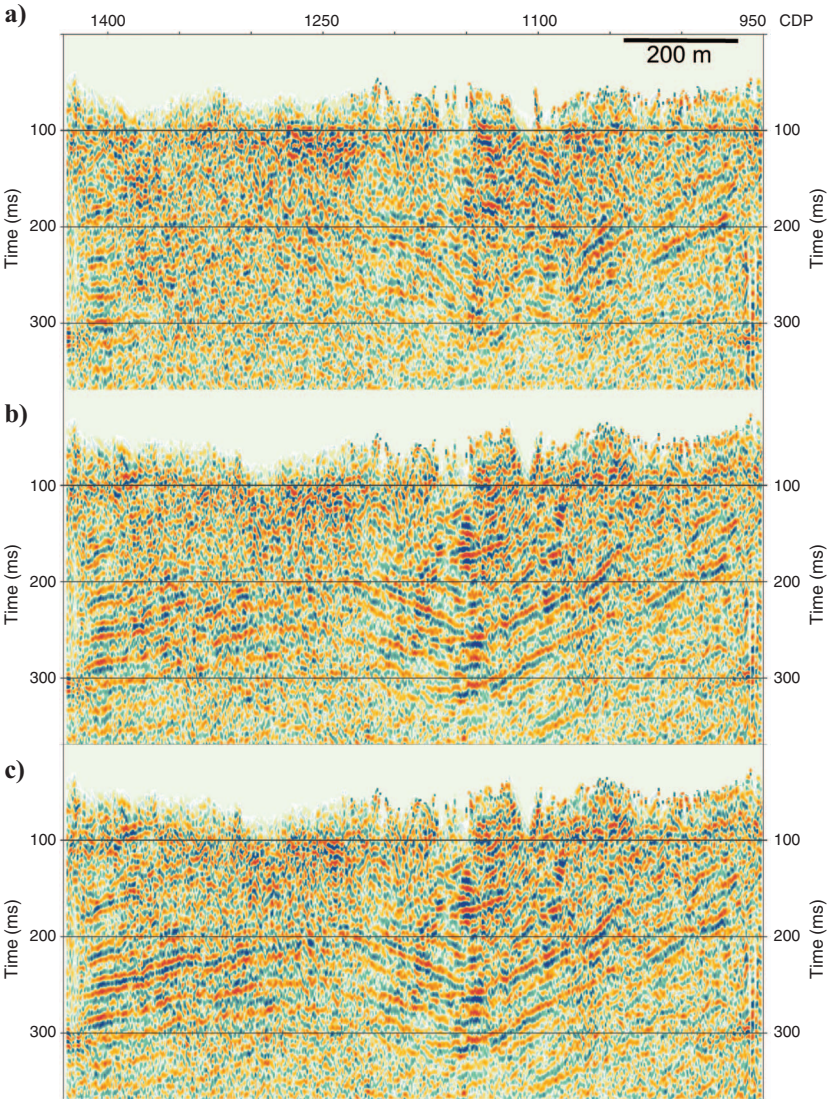

Figure 15. Sections of the land-land data at the floating datum obtained with the final stacking velocity field (a) before the application of the refraction statics correction, (b) after their application, and (c) after a final correction of residual statics. The progressive increase of the continuity of the reflectors is evident.

vironment, and obviously, the nature of the subsurface with continuous undeformed layers and smoother lateral velocity variations.

The land-marine segment (CDP 896–953 in Figure 16) suffers a strong decrease of coverage, caused by the combined effect of the limited number of shot records contributing to the stack and by the muting of overstretched reflections. Its response is, however, quite similar to the land-land stack (CDP 954–1421 in Figure 16), which investigates the main landslide body. Continuous deep reflections, overlaid by disrupted reflections and chaotic events, are evident here.

Depth migration

The quality of the time stack section shown in Figure 16 allows an interpretation of the structure of the landslide body, but its vertical timescale does not permit a straightforward use by engineers and geologists for further study and consolidation plans. In addition, it prevents an easy correlation with the information brought in by tens of boreholes drilled in the area, although most of them are limited to shallow depths. Thus, in addition to the known imaging issues of the correct positioning of reflectors, a depth-migrated profile is, in this case, a necessity for enabling a thorough use of the reflection data.

We tested prestack depth migration (PSDM), but the results were unsatisfactory: notwithstanding the efforts for improving the S/N, the noise still present in the common-offset data degraded the outcome of migration. Thus, PSDM was not applied to the data. On the contrary, the fair quality of the final stack section allowed a good performance of poststack depth migration with a Kirchhoff algorithm. Figure 17 shows the complete depth section with, overlaid, the (smoothed) velocity field derived from traveltime tomography of refracted and reflected events. We derived the starting velocity model from the smoothed stacking velocity field. Final velocities range from 800 m/s at the surface through 2200 m/s at depth, with the main body of chaotic reflections (above the coherent, "spoon-shaped" horizon starting at an elevation of −10 m on the left-hand side of Figure 17) characterized by velocities of about 1900–1950 m/s. However, significant lateral variations occur, especially in the central portion of the land profile (between CDP 1100 and 1250) where the velocity reaches 2100 m/s. The location of this velocity increase is coincident with the occurrence of segments of coherent reflections (about CDP 1150 at −50 m in Figure 17), which indicate the presence of competent elements surrounded by a mélange of chaotic material.

Figure 17, on the right-hand side, shows a segment of a pre-existing seismic line. This line is part of the marine seismic grid mentioned in the introduction, and constitutes a seaward prolongation of our profile (see Figure 1). We depth migrated this extension using a velocity field extrapolated from our data.

Although some boreholes were drilled in the area, most of them reached only the shallower portion of the landslide, and downhole velocity measurements were carried out in just a few of them. Thus, no information from wells was used to drive migration. Instead, before producing the final result, we ran some tests with different migration parameters and different smoothing of the velocity field.

RESULTS

A clear delineation of the subsurface structure both on- and offshore results from the seismic sections of Figures 16 and 17.

The syncline upon which the landslide is seated, and which is suspected to have a role in the rock-mass movements of the area, is observed clearly. The layers at its north (seaward) flank nicely match the correspondent layers present on the pre-existing seismic line (Figure 17). This structure conforms to a larger-scale synclinal structure (Tavernelle syncline), which is shown by seismic profiles for hydrocarbon exploration and by land geologic surveys (Ciancetti et al., 1986; Cotecchia, 1997). From the ensemble of these data, it can be seen that the syncline axis, from bottom to top, shifts slightly northward and maintains a slant orientation (east-southeast–west-northwest in relation to the coastline.

On a smaller scale, the main target of our study was to discern the geometry of the deepest possible detachment surface and in particular its maximum depth and its emergence at the landslide foot. To this end, a key criterion for interpretation is the chaotic or continuous nature of the reflections: chaotic reflections and scattering occur within the landslide body, and continuous reflections underneath, unaffected by the mass movements, indicate potential sliding surfaces. The adjective "potential" is used here to underline the fact that the seismic image gives a static representation of the subsurface and thus, from seismic images alone, it is possible to assess only indirectly whether mass movements have been, and/or are presently, active.

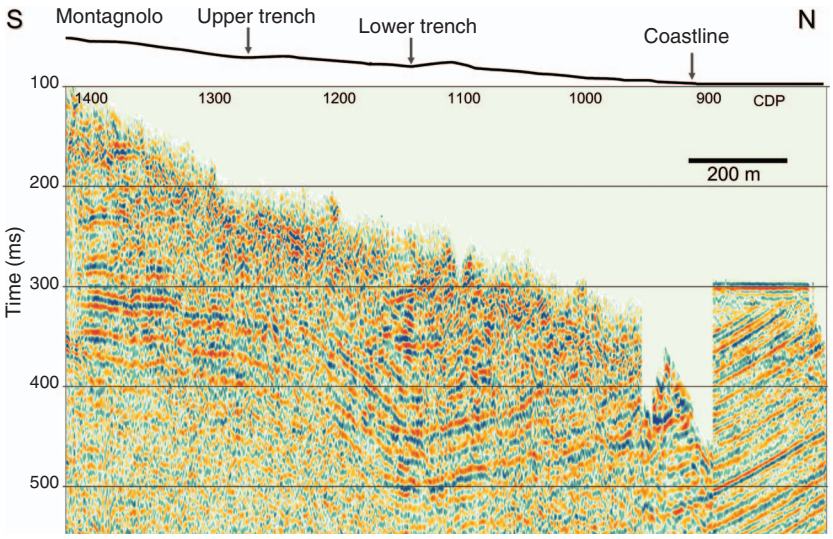

Figure 16. Final stack section to the final datum at 250 m a.s.l. From left to right: the land-land data, CDP 1421-954; the land-marine data, CDP 953-896; the marine-marine data, CDP 895-802. Note the different characteristics of the data although at the end of the time processing. The marine-marine stack shows the highest resolution and deeper penetration. The land-marine stack at shallow times suffers from the NMO stretch mute. On the land-land data, continuous deep reflections overlaid by disrupted ones are evident.

Therefore, the continuous reflections in Figures 16 and 17 forming the top of the syncline structure, which are interrupted partly by small faults, represent the deepest possible detachment surface. Biostratigraphic information from boreholes dates this horizon to the near Top Lower Pliocene. This "spoon-shaped" reflector can be followed from the apical part of the landslide area to the coast.

Figure 18 shows a close-up of the stack section in the apical part. Stack time data are shown here, because at the edge of the profile they have a better quality than the correspondent depth-migrated data. Note the presence of shallow continuous horizons that pass laterally to a zone of chaotic reflections. This transition corresponds to the first detachments at the hilltop. Underneath, the near Top Lower Pliocene reflection remains continuous below the chaotic zone, and it can be followed downhill in the close-up of the depth-migrated section in Figure 19.

The near Top Lower Pliocene horizon reaches its deepest point, about 120 m below sea level, at around CDP 1133 where it starts rising toward the coast (Figures 17 and 19). Above it, an ensemble of scattered events surrounds discontinuous segments of coherent reflections that seem to be involved in the mass movement. In addition, in the shallow portion of the section, small concave-upward horizons are evident. These coincide with smaller sliding surfaces pertinent to minor and collateral landslides known from previous investigations (Cotecchia, 1997), although migration artifacts (smiles) cannot be excluded as the cause of these features.

Finally, the subsurface setting near the coast, an area that is crucial for engineering planning, is shown in detail in Figure 20. Again, in Figure 20, a close-up of the time stack section is shown because of its sharper reflections and discontinuities. However, the depth section gives us the same indication. The dipping and parallel reflectors of the northern flank of the syncline are undeformed and truncated at their top by a near-horizontal discontinuity, which biostratigraphic records date at the Holocene. Above this unconformity, also to appear undisturbed, are the seafloor and a wedge of layers, which constitutes the expression of a progradational sedimentation — better seen farther offshore in the pre-existing seismic line (see Figure 17). This setting shows that at least since the Holocene this area has not been subjected to any kind of deformation; thus it indicates that the position of the landslide foot is closer to the coast.

DISCUSSION

The simultaneous land-marine acquisition carried out across the Ancona landslide provides an abundance of data that can be processed effectively to yield seismic images of significant value for engineering and geologic purposes. In addition, the adopted undershooting configuration allows the bypassing of the Flaminia road and of the coastal railway, and the illumination of the targets there below.

However, notwithstanding the acquisition effort, the main problem affecting the field data is noise of various types and at varying amplitude levels. Environmental disturbances caused by road, railway, and marine traffic, to nearby broadcasting antennas and seismic-generated noise such as air-gun bubble reverberations and surface waves, all produce severe contamination. These issues, along with the rugged topography and with the complexity of the landslide mass, make the imaging of the subsurface a difficult task. It is because of the high data redundancy, high dynamic range of the recording equipment, and targeted processing that a good quality of the final time and depth seismic sections is achieved. These show clear and detailed images of the subsurface, which can be interpreted reliably by engineers and geologists, and which constitute an input for consolidation plans.

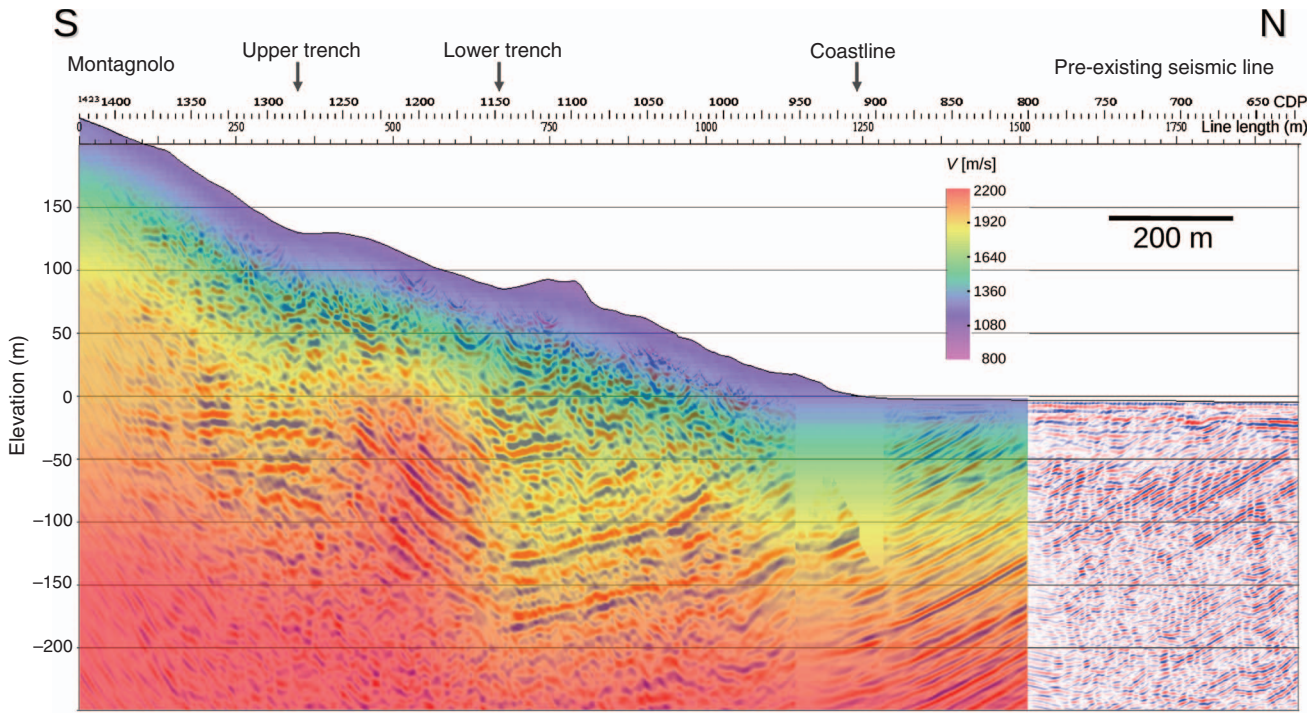

Figure 17. Kirchhoff poststack depth migration of the stack section in Figure 16 overlaid by the velocity field derived from tomography. On the right, a portion of a pre-existing marine seismic line is included and a fair match with the new line is observed. On the depth section, the syncline structure, with its depocenter on land (below CDP 1133), is clearly visible.

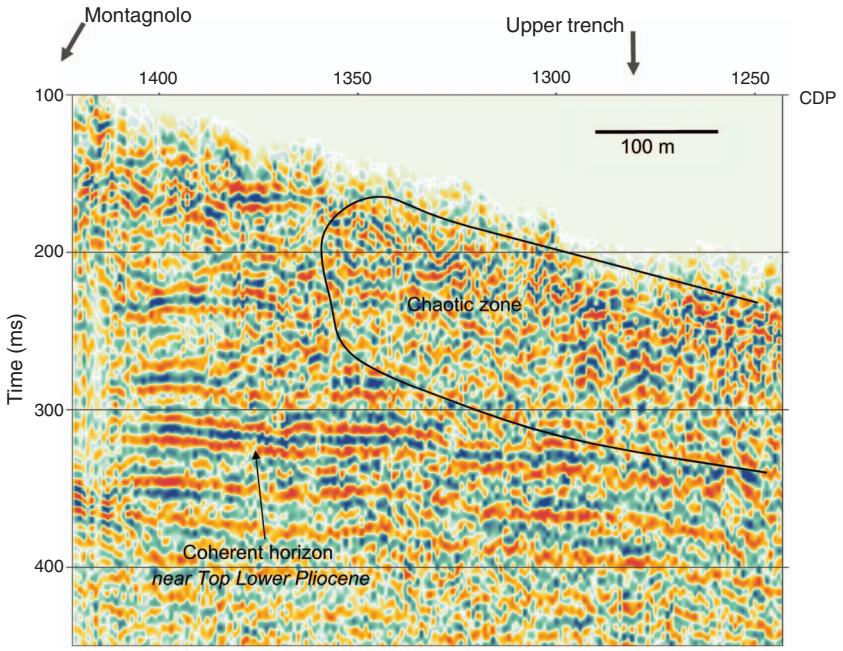

Figure 18. Close-up of the stacked section in the apical part of the seismic profile, near the Montagnolo locality. Note the shallow continuous horizons that pass laterally to a zone of chaotic reflections. This transition corresponds to the first detachment at the hilltop.

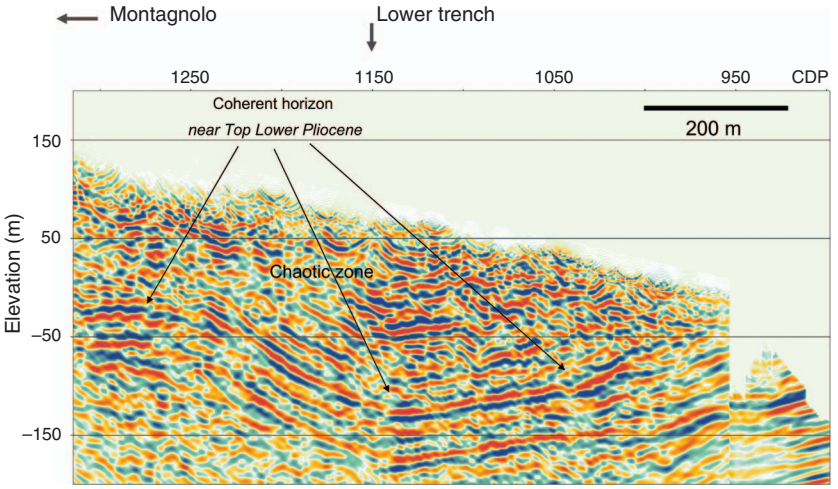

Figure 19. Close-up of the depth-migrated section in the central part of the seismic profile. The coherent horizon named near Top Lower Pliocene can be followed from below the chaotic zone at the south (Figure 18) through its deepest point about 120 m below sea level at CDP 1133, and farther on toward the coast, where it rises again. Along with the underlying reflections, it clearly delineates the Tavernelle syncline structure. Chaotic reflections and scattering occur above this event, suggesting this horizon as the deepest possible detachment surface.

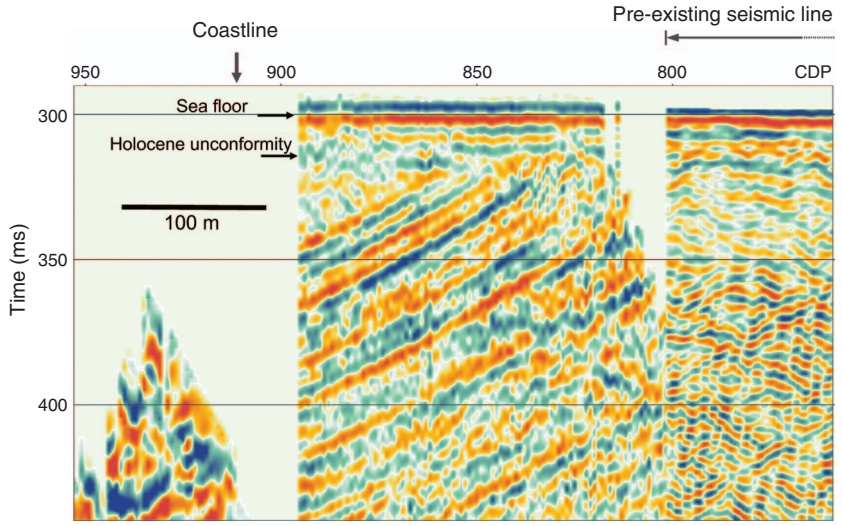

Figure 20. Close-up of the stacked section showing the subsurface setting at the coastal area. The dipping and parallel reflections of the northern flank of the syncline as well as the seafloor appear undisturbed, indicating that this area has not been subjected to any kind of deformation in recent years.

The rupture surface is particularly evident in the apical part of the landslide, and it can be traced downdip where it becomes coplanar with the top of the syncline structure. The deep sliding surface reaches its maximum depth in correspondence with the lower trench, at about 200 m below the topographical surface, quite a greater depth than previously predicted. In addition, the uncertainty of the location of the emergence of the deep detachment surface is reduced to a short segment between the coast and 30 meters offshore. Instead, farther off the coast, where it was supposed previously that the deep detachment surface emerged, the near seafloor sediments lie undisturbed.

CONCLUSIONS

Considering the complications resulting from noise, which affected the original data, and the complexity of the landslide mass, we view the results of this experiment as satisfactory.

Indeed, the seismic imaging of landslide bodies often is a challenge for seismic reflection, but this work shows that properly planned, acquired, and processed seismic reflection surveys can yield usable results even in difficult conditions, such as those of the Ancona landslide.

However, it should be pointed out that our seismic sections depict a 2D image of the subsurface that cannot safely be assumed to extend laterally along the whole coastal front affected by the landslide. This is more so because, as also demonstrated by previous studies, the structural features of the area, such as the syncline axis, have a slant orientation with respect to the coastline. This is of special importance for the location of the emergence of the deep sliding surface offshore because the distance from the coastline could vary along the landslide front.

Thus, to evidence the true tridimensional geometry of the landslide body, a 3D seismic survey would be necessary.

ACKNOWLEDGMENTS

The present work has been carried out in the framework of the following research projects: Monitoring Urban Subsidence, Cavities, and Landslides, funded by the European Union, and Geophysical study and monitoring of the landslide phenomena in the Ancona area, funded by the Ancona Municipality. We wish to thank the Ancona Municipality and the technical staff of the City of Ancona for their support throughout these projects. Thanks are due to our project partners Politecnico di Milano, TeleRilevamento Europa, and Istituto Nazionale di Oceanografia e Geofisica Sperimentale, and to all our M.S. and Ph.D. students who took part in the acquisition and processing of the data, in particular to Simone Baudo, now at ENI E&P. We also acknowledge Professor Vincenzo Cotecchia for his scientific support on the engineering side and the many useful discussions had in Ancona.

We thank an anonymous reviewer and Mark Vardy, who contributed to improve the readability and clarity of the paper.

The seismic processing was carried out with the ProMax software of the Landmark Graphics Corporation.

REFERENCES

Baker, G. S., 1999, Processing near-surface seismic-reflection data: SEG.

Bernardini, M., U. Crescenti, M. Rainone, N. Sciarra, and G. S. Tazioli, 1986, La campagna geognostica: Studi Geologici Camerti, special volume, La grande frana di Ancona del 13 Dicembre 1982, 95–119.

Bianco, B., 1986, Rilievi inclinometrici: Studi Geologici Camerti, special volume, La grande frana di Ancona del 13 Dicembre 1982, 121–126.

Bichler, A., P. Bobrowsky, M. Best, M. Douma, J. Hunter, T. Calvert, and R. Burns, 2004, Three-dimensional mapping of a landslide using a multigeophysical approach: The Quesnel Forks landslide: Landslides, **1**, 29–40.

Brückl, E., J. Brückl, and H. Heuberger, 2001, Present structure and prefailure topography of the giant rockslide of Köfels: Zeitschrift für Gletscherkunde und Glazialgeologie, **37**, Heft, 1, S.49–79.

Bruno, F., and F. Martillier, 2000, Test of high-resolution seismic reflection and other geophysical techniques on the Boup Landslide in the Swiss Alps: Surveys in Geophysics, **21**, 333–348.

Calamita, F., and G. Deiana, 1986, Geodinamica dell'Appennino umbro-marchigiano: Memorie della Societa Geologica Italiana, **35**, 311–316.

Cancelli, A., F. Marabini, M. Pellegrini, and G. Tonetti, 1984, Incidenza delle frane sull'evoluzione della costa adriatica da Pesaro a Vasto: Memorie della Societa Geologica Italiana, **27**, 555–568.

Cassinis, R., I. Tabacco, G. F. Bruzzi, C. Corno, A. Brandolini, and E. Carabelli, 1985, The contribution of geophysical methods to the study of the great Ancona landslide (December 13, 1982): Geoexplorarion, **23**, 363–386.

———, 1986, Indagini geofisiche: Studi Geologici Camerti, special volume, La grande frana di Ancona del 13 Dicembre 1982, 83–93.

Ciancetti, G. F., U. Crescenti, and T. Nanni, 1986, Caratteristiche geologiche: Studi Geologici Camerti, special volume, La grande frana di Ancona del 13 Dicembre 1982, 25–27.

Coltorti, M., F. Dramis, B. Gentili, G. Pambianchi, and M. Sorriso-Valvo, 1986, Aspetti geomorfologici: Studi Geologici Camerti, special volume, La grande frana di Ancona del 13 Dicembre 1982, 29–39.

Cotecchia, V., 1997, La grande frana di Ancona: Atti Convegni Lincei, **134**, 187–259.

Curzi, P. V., and A. Stefanon, 1986, Indagini a mare: Studi Geologici Camerti, special volume, La grande frana di Ancona del 13 Dicembre 1982, 135–144.

Martinez, J. F., J. Cartwright, and B. Hall, 2005, 3D seismic interpretation of slump complexes: Examples from the continental margin of Israel: Basin Research, **17**, 83–108.

Mazzotti, A., and F. Rocca, 2003, Satellite radar interferometry and reflection seismic: An integrated geophysical study on the great Ancona Landslide, 9th Meeting, Environmental and Engineering Geophysics, 2003, O006-1–O006-4.

Rott, H., T. Nagler, F. Rocca, C. Prati, A. Mazzotti, H. Keusen, S. Liener, and D. Tarchi, 2003, InSAR techniques and applications for monitoring landslides and subsidence, *in* T. Benes, ed., Geoinformation for European-wide integration, Proceedings of the 22nd EARSeL Symposium, Prague, June 2002: Millpress, 25–31.

Schnellmann, M., F. S. Anselmetti, D. Giardini, and J. A. McKenzie, 2006, 15,000 years of mass-movement history in Lake Lucerne: Implications for seismic tsunami hazards: Eclogae Geolicae Helvetiae, **99**, 409–428.

Stucchi, E., F. Zgur, and L. Baradello, 2005, Seismic land-marine acquisition survey on the Great Ancona Landslide: Near Surface Geophysics, **3**, 235–243.

Yilmaz, O., 2001, Seismic data analysis: I — Processing, inversion, and interpretation of seismic data: SEG.